Supplementary Information

Supplement Text

S.1 Vegetation growth in QUINCY

Vegetation growth in QUINCY is calculated as the minimum of source (i.e., photosynthesis, derived at half-hourly timestep with a state-of-the art coupled photosynthesis-stomatal model accounting for a vertically resolved canopy) and sink limitation (growth of new tissue constrained by plant labile N and P, as well as vegetation temperature and moisture). Short-term fluctuation (days) between source and sink limitations are buffered through labile carbon and nutrient pools. Vegetation nutrient uptake is driven by available C for growth and tissue stoichiometry, where dynamic plant stoichiometry enables for adaptation of plants to low nutrient levels (Caldararu et al., 2020). Nutrient uptake is limited by several factors, including fine root biomass and solute nutrient concentrations of the respective soil layer.

S.2 Nutrient Cycling in QUINCY

The model includes a comprehensive representation of nitrogen fluxes in the soil, including the production of the nitrogen gases such as N_2O and N_2 through nitrification and denitrification as a function of solute NH_4 and NO_3, labile soil organic carbon, soil temperature and soil moisture, which in turn affects the fraction of the soil that is aerated. Thereby, NH_4 that is available upon organic matter degradation can be transformed to NO_3 via nitrification under aerobic conditions. The process also releases a small fraction of N_2O. NO_3 can be further used for microbial metabolic activities under anaerobic conditions, producing the gases N_2O and N_2. The model does not consider intermediate forms of nitrogen in both nitrification and denitrification processes.

QUINCY also incorporates a full representation of the phosphorus cycle, in particular simulating exchanges of primary, solute, absorbed and occluded phosphorus in the soil (Thum et al., 2019; Yu et al., 2020). Phosphorus sorption capacity depends on mineral and organic material in each soils layer and is affected by soil temperature and moisture.

S.3 QUINCY extensions for high latitudes: Soil Freezing

The soil module in QUINCY previously considered surface exchange through net radiation balance R_{net}, latent heat from evapotransporation $H_{latent,evapotrans}$, and vertical heat transfer G as a result of heat conductance through the soil. For this study, we extended the soil layer heat balance, which is solved implicitly in the model. Thus, the update of soil layer temperatures at every model timestep, takes into account the freezing and melting of soil water, and its impact on latent heat. For the surface exchange this extends the budget to:

$$(1)\ C_S \frac{\partial T_S}{\partial t} = R_{net} + H_{sensible} + H_{latent,evapotrans} + H_{latent,freezethaw} + G$$

With T_s being the surface soil temperature, C_S the volumetric heat capacity of the layer adjusted for soil layer width in J m^{-2} K^{-1}. R_{net} is the net radiation with positive values meaning a flux towards the soil in J m^{-2} s^{-1}. $H_{sensible}$ is the heat flux from sensible heat exchange with

the atmosphere, $H_{latent,evapotrans}$ is the evapotranspiration flux, and $H_{latent,freezethaw}$ is the latent heat flux from freezing and thawing of soil, all in J m^{-2} s^{-1}.

The heat budget in the sub-surface soil is governed by the vertical soil ground heat flux G and latent heat fluxes. Temperatures in the subsurface soil T_s were computed through conductive transfer with heat conductivity constant λ_s (J K^{-1} s^{-1}) and corrected for latent heat fluxes due to evapotranspiration and freezing/thawing of soil in every layer:

$$(2)\ C_S \frac{\partial T_{Soil}}{\partial t} = \frac{\partial}{\partial z}\left(-\lambda_s \frac{\partial_T}{\partial z}\right) + H_{latent,evapotrans} + H_{latent,freezethaw}$$

Where ∂z was the difference between the center points of the soil layers in m.

We considered $H_{latent,freezethaw}$ from the fusion phase change (freezing/melting) of water change both for the surface heat budget, as well as for the subsurface soil layers. In similarity to implementations in JSBACH3 (Ekici et al., 2014), we considered a threshold of supercooled water that cannot undergo a phase change to ice. We defined this threshold as 1/5th of the soil layer field capacity as a result of analysed soil moisture observed at the Cherskyi site (Supplement Figure S1). After subtracting this supercooled water volume, the potentially available for freezing in every soil layer is therefore given as:

$$(3)\ V_{w,available} = \frac{\partial(V_{w,soil} - V_{w,supercooled})}{\partial t}$$

In the model, we use water volumes per area with unit m^3 m^{-2}. The supercooled water fraction was estimated to be 0.2 of the saturated capacity of the soil (Supplement Figure S1). Pragmatically, however, this supercooled liquid water needed to be kept at levels above the permanent wilting point at depths at less than 20 cm in order for vegetative organs to survive the winter.

If the temperature of the soil layer decreased below the freezing point and liquid water susceptible to freezing ($V_{w,available}$) is still present in the soil, the amount of liquid water that froze was derived by first computing the heat difference ΔH of the soil layer temperature, after accounting for the ground heat flux to the layer, and the freezing point temperature. If the cooling given by ΔH is larger in magnitude than cooling needed to freeze the entirety of soil water susceptible to freezing $V_{\mathrm{w,available}}$, F_{freeze} (m s-1) is equal to $V_{w,available}$ and the rest the heat deficit reduces the soil layer temperature after accounting for the latent heat flux from freezing (Equation 9):

$$(4)\ F_{freeze} = \frac{\partial V_{w,available}}{\partial t}$$

If the cooling determined by ΔH is insufficient to freeze all the water of a soil layer, the amount of water that freezes was calculated as following in every individual soil layer:

$$(5)\ F_{freeze} = \frac{\Delta H}{L_{fV,w}}$$

With $L_{fV,w}$ being the volumetric latent heat of water in J m^{-2}. In this case temperature remains at the freezing point (273.15 °K), and liquid water content is reduced by the freezing flux F_{freeze}.

If ice is present in a soil layer, and the temperature resulting from Equation (2) would exceed the freezing point after accounting for the groundheat flux G_s, ΔH is calculated as the heat excess past freezing point. If ΔH is larger in magnitude than the heat required to melt soil layer water content V_{ice}, the amount of ice that is melted is given by V_{ice} given as a negative flux F_{freeze}:

$$(6)\ F_{freeze} = -\frac{V_{ice}}{\partial t}$$

If ΔH is not large enough in magnitude to melt soil layer ice content m_{ice}, the amount of ice that is melted is calculated as:

$$(7)\ F_{freeze} = -\frac{\Delta H}{L_{fV,w}}$$

After determining F_{freeze}, soil layer water content V_w , soil layer ice content V_{ice} and soil layer temperature T_{soil} are updated:

$$(8)\ \frac{\partial V_w}{\partial t} = F_{freeze}$$

$$(9)\ \frac{\partial V_{ice}}{\partial t} = -F_{freeze}$$

$$(10)\ \Delta T_s = \frac{\Delta H + L_{fV,w} * F_{freeze}}{C_s * h_s}$$

With h_s being the width of the soil layer in m.

S.4 QUINCY extensions for high latitudes: Snow dynamics

We represented snow dynamics in a 5-layer scheme, for which we considered flows of heat and water within and between the snow layers. We assumed a minimum snow depth threshold of 2 cm, at which the snow coverage of an individual layer starts to affect soil

surface energy fluxes. From 2 cm to 5 cm snow depth, we compute a fraction at which the snow affects the surface heat exchange from nil to one, the rest of the surface heat exchange is driven by bare soil surface heat exchange. The snow layers were constrained to a maximum height of 5 cm, except for the top layer, which can exceed this threshold infinitely. The snow surface heat exchange was solved implicitly, as for the soil:

$$(10)\ C_{Snow}\frac{\partial T_{Snow,surf}}{\partial t} = R_{net,snow} + H_{sensible,snow} + H_{latent,snowevaporation} + H_{latent,snowmelt} + G_{snow}$$

C_{Snow} is the volumetric heat capacity of snow scaled to the snow layer height J m^{-2} , T_{snow} being the snow surface layer temperature, $R_{net,snow}$ the net radiation flux to the snow, $H_{sensible,snow}$ the sensible heat flux to the snow, $H_{latent,snowevaporation}$ the latent heat flux from snow sublimation, $H_{latent,snowmelt}$ the latent heat flux from snow melting, and G_{snow} is the vertical heat flux, all in J m^{-2} s^{-1}. The snow surface layer was determined dynamically at every timestep, being the top snow layer where the snow height threshold of 2 cm was exceeded. Snow was thereby assumed to reflect radiation with the albedo constant of 0.6 for both NIR and VIS.

We assumed that the transfer of heat through snow layers was driven by conductivity, with specific heat conductivity and specific heat constants given in Table 1. The transfer of heat between snow layers was assumed to be dominated from fluxes as a result of conductance, for which we assumed a single constant (Table 1). Snow layer temperatures below the snow surface layer were computed as a result of the heat transfer and the single heat capacity used for every layer (Table 1).

$$(11)\ C_{Snow}\frac{\partial T_{Snow}}{\partial t} = \frac{\partial}{\partial z}\left(-\lambda_{snow}\frac{\partial T_{snow}}{\partial z}\right) + H_{latent,snow}$$

Heat exchange between snow and soil was considered through conductivity between the bottom snow layer and the first soil layer. Thus, the heat exchange there was computed as the flux between the bottom snow layer and the top soil layer, using the heat conductivity constant of snow.

For temperatures at and above freezing point, we assumed phase change of snow to liquid water and calculated the latent heat flux originating from the phase change. This was done exactly as for the soil latent heat flux from thawing, but without a supercooled liquid water fraction. We also did not represent water re-freezing with the snow column, thus liquid water infiltrated the soil, or was re-routed to the surface runoff flux in the case that the soil was already saturated, directly after melting.

S.5 QUINCY extensions for high latitudes: Inundation

Soil freezing disturbs water flows in the soil, effectively inhibiting vertical transfer of water past frozen soil depths and thus retaining moisture in the top soil (Walvoord and Kurylyk, 2016). We considered the physical inhibition of flow through frozen layers once their ice water mass reached field capacity. We furthermore represented inundation above the permafrost layers. Since there were generally no downward flows past the permafrost layer depth, water accumulates above the permafrost layer in the spring thaw season (Supplement Figure S2).

Drainage of the deepest soil layer was set to nil if it was frozen, causing water to eventually accumulate in soil layers above saturated frozen layers. In soil layers above the permafrost layers, liquid water accumulates in periods of large fluxes of water to the soil (e.g., snow melt), causing saturated conditions through the whole soil column as found in observations in spring/early summer (Supplement Figure S2). Liquid water from snow melt was added to the top soil layer, without considering refreezing within the snow column.

S.6 Construction of GPP product for the Samoylov site

For the site on Samoylov Island, we used the dataset of net eddy covariance CO_2 fluxes which was made publicly available by Holl et al. 2019b and further processed it to obtain partitioned CO2 fluxes, namely separate half-hourly time series of gross primary production (GPP) and total ecosystem respiration (TER) for the months from May up to and including September. We used a refined version of the bulk model approach presented by Runkle et al. 2013 by fitting a combined photosynthesis-respiration model to consecutive subsets of flux data from within 2-day windows in order to obtain parameter time series instead of fixed NEE model parameters over the course of a vegetation period. We then linearly interpolated the resulting parameter time series with two days resolution to one-day steps and approximated the course of a smooth parameter curve with the same temporal resolution using an infinite impulse response lowpass filter with a cutoff frequency of 90 days from the Matlab v9.7 Signal Processing Toolbox. A similar method has been applied by Holl et al. 2019a who could also show good agreement with bulk model parameter estimates from manual chamber measurements which were interspersed throughout an eddy covariance observation period. To estimate half-hourly TER and GPP flux time series, we used half-hourly observations of air temperature and photosynthetically active radiation to drive the previously determined daily model versions. We filled remaining gaps using a wider range of half-hourly observations of meteorological and soil variables and artificial neural network ensembles following Holl et al. 2020. This approach uses multilayer perceptions with a single hidden layer and includes an input selection algorithm as well as a complexity reduction routine to minimize the number of hidden layer nodes.

S.7 Estimation of N and P limitation for vegetative growth

In order to estimate the timing and magnitude of N and P limitation on vegetation growth, we used the built-in model output of relative plant P and N demand (Supplement Text S1,

Thum et al., 2019). This expresses the ratio between plant P and N demand, which plants already adapt to soil conditions, to soil P and N availability. Thus, these values indicate stronger nutrient limitation the closer to 1 they are.

S.8 The Chokurdakh site

The Chokurdakh is located near the Indigirka River. The site is subject to continental climate since it is situated 150 km away from the coast. The soil is covered by around 20 cm of organic peat (van der Molen et al, 2017). The vegetation at the site is generally dominated by mosses, graminoids and grasses. We used site-level eddy-covariance GPP estimates as described in van der Molen et al (2007) for the years 2008-2011 (available under FLUXNET2015 dataset, Pastorello et al., 2015).

Supplement Figures

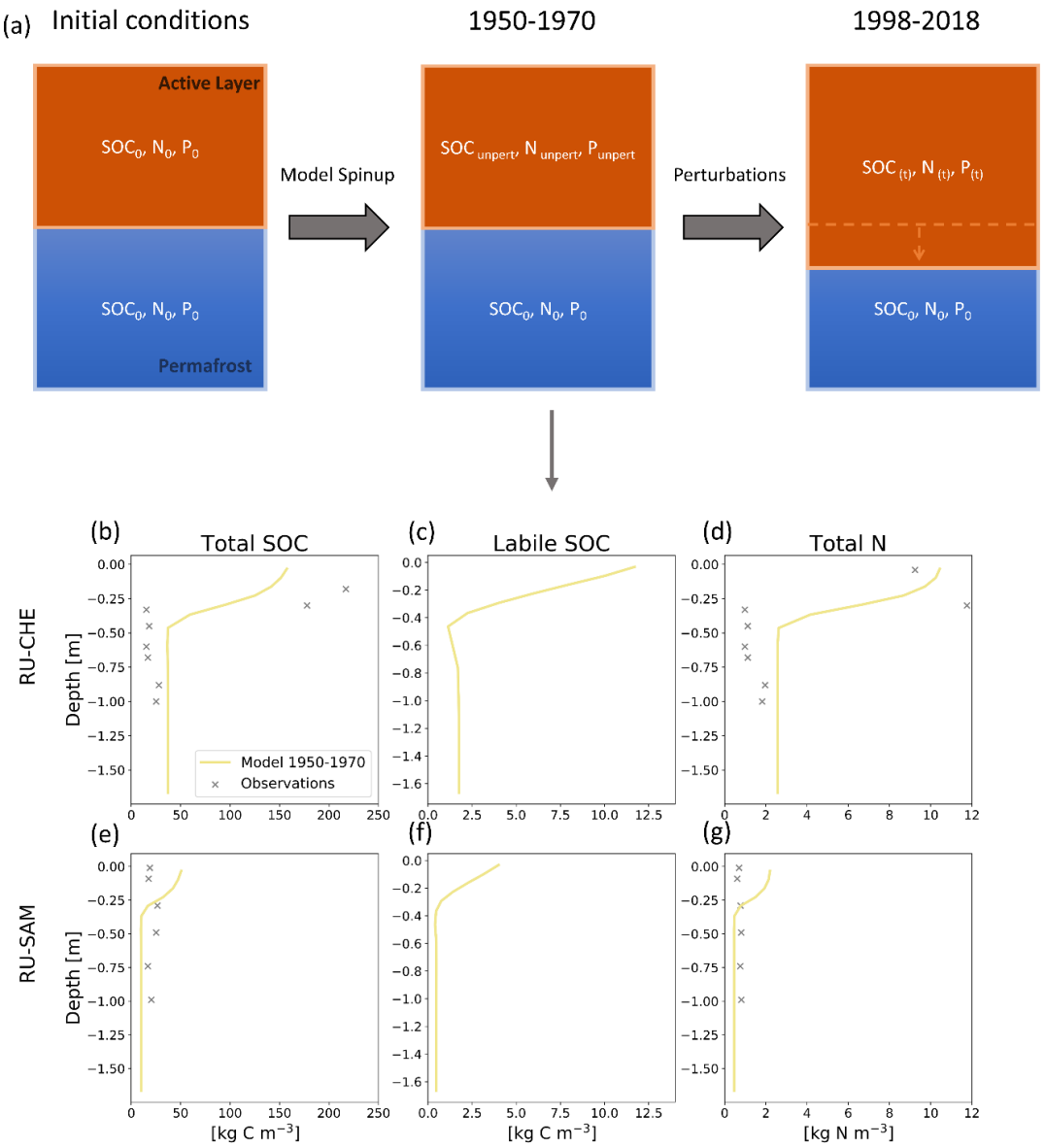

Supplement Figure S1. Panel (a) shows a scheme of our initialisation strategies for biogeochemical soil variables for a better representation of the permafrost, with SOC, N and P as simplifications for all soil organic C (SOC), N and P compounds, respectively. Note that in the model, these contents can vary with depth within the active layer, as well as at permafrost depths. Initial conditions show the variables (SOC_0, N_0, P_0) prescribed to the model before the spin-up simulations. Spinning up the model from initialisations leads to an assumed unperturbed state. SOC, N and P remain essentially constant below the active layer depth during this spin-up period, whereas above-freezing temperatures equilibrates SOC_{unpert}, N_{unpert} and P_{unpert} in the unfrozen layers above. Changes in atmospheric conditions in the simulations from 1901-2018 trigger changes in biogeochemistry in the active layer that can change in depth (perturbed state) leading to perturbed soil contents $SOC_{(t)}$, $N_{(t)}$ and $P_{(t)}$. Lower panels b-g show simulated vertical profiles of total SOC (b,e), labile (fast) SOC (c,f) and total soil N (d,g) compared to total SOC and total N observations at the Cherskiy (RU-CHE, top row) and Samoylov (RU-SAM, bottom row) sites, respectively.

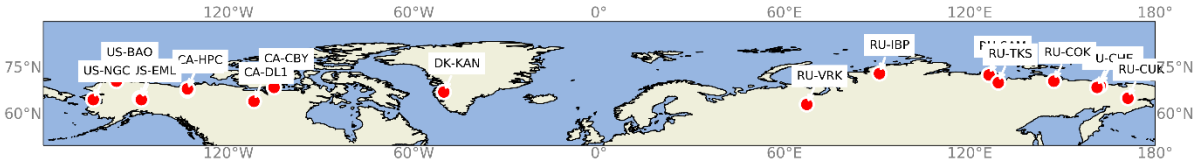

Figure S2. 15 grassland sites chosen across the high-Arctic region with Fluxnet identifications (Pallandt et al., 2021, Supplement File higharctic_sites_1990-2019_list2022-04-21.dat).

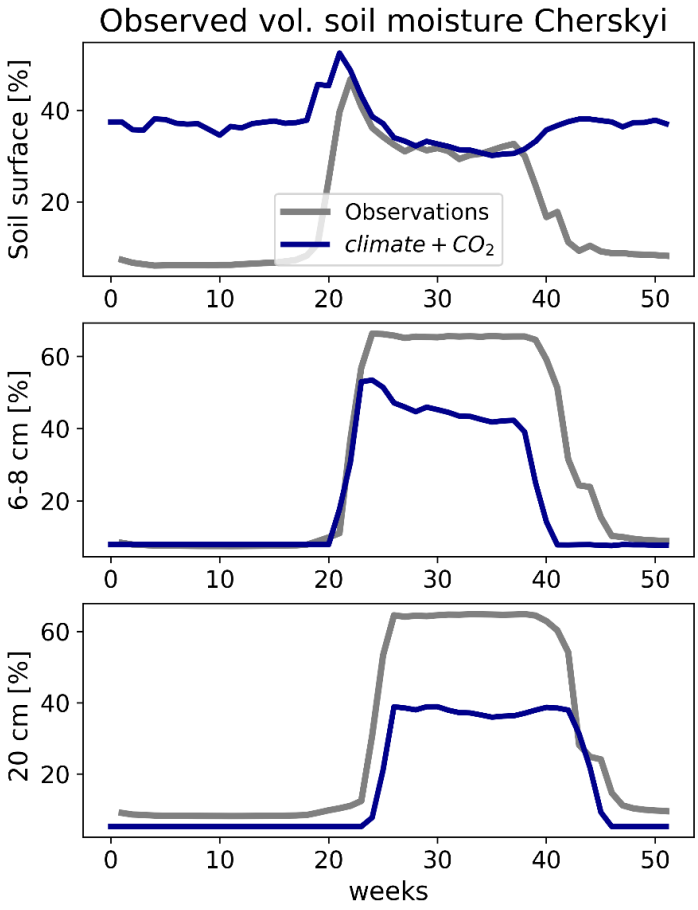

Figure S3. Relative soil moisture averaged over 2015-2019 at the Cherskiy site derived from our model simulations (blue) and observations (grey).

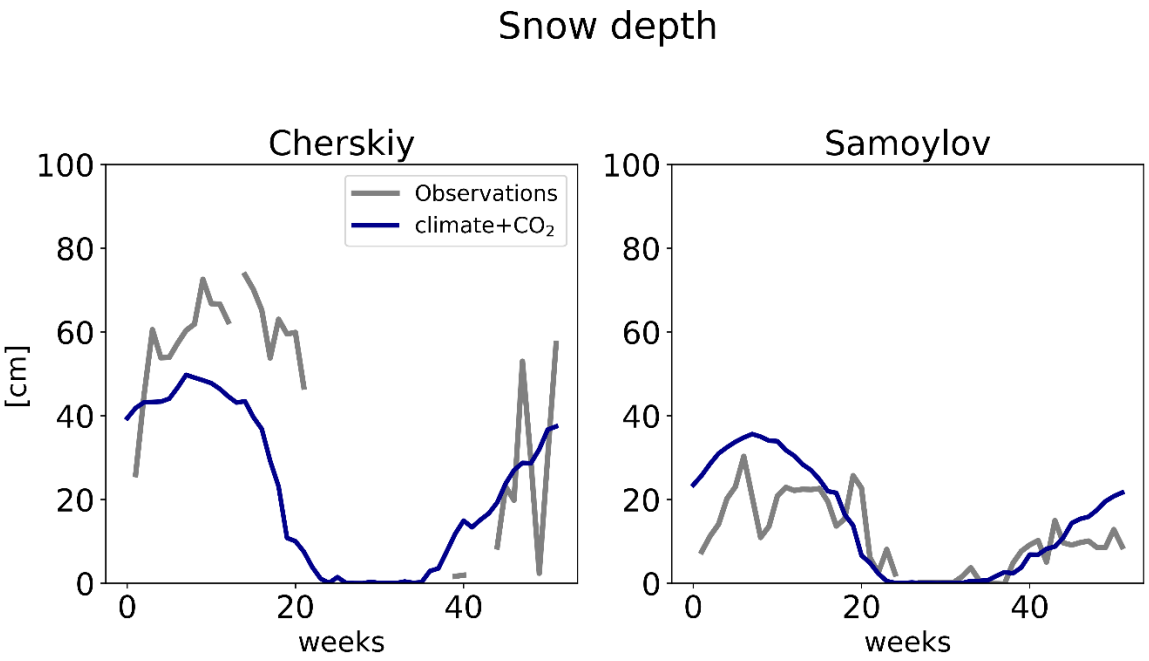

Figure S4. Observed snow depths at Cherskiy and Samoylov over 2015-2018 and 2009-2015, respectively.

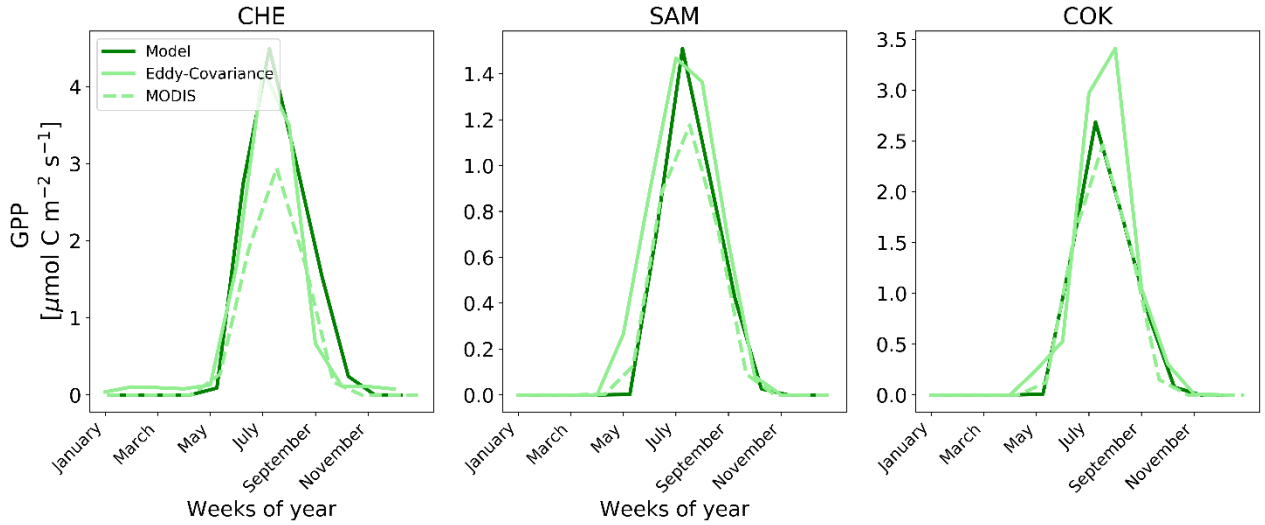

Figure S5. Monthly means of observed (eddy covariance-derived, MODIS product) and simulated GPP at Cherskiy, Samoylov and Chokurdakh sites over 2015-2018, 2009-2015 and 2008-2010, respectively.

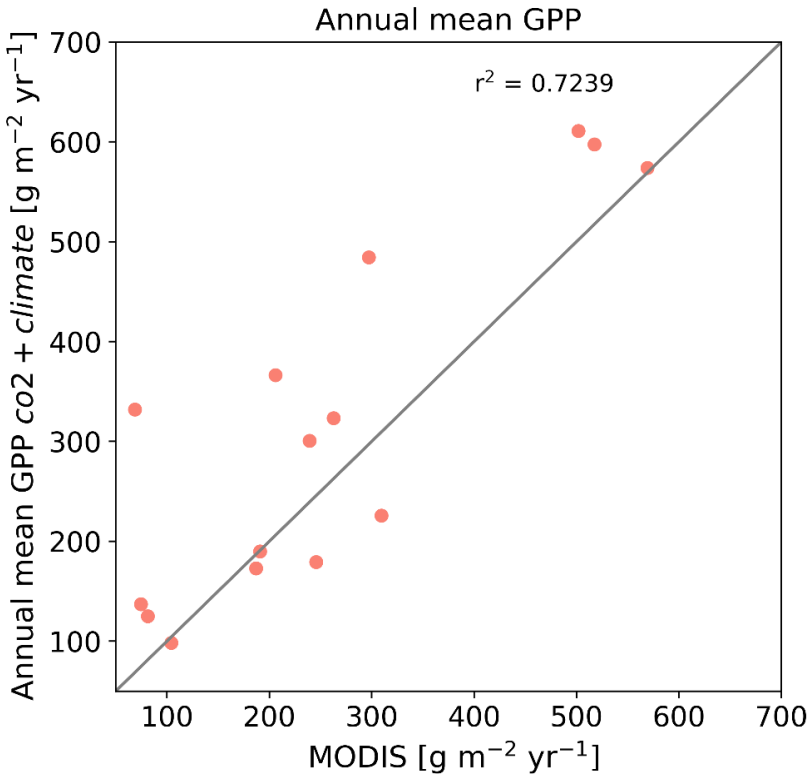

Figure S6. Simulated annual mean GPP against observed annual mean GPP MODIS Terra GPP for all individual high-Arctic sites.

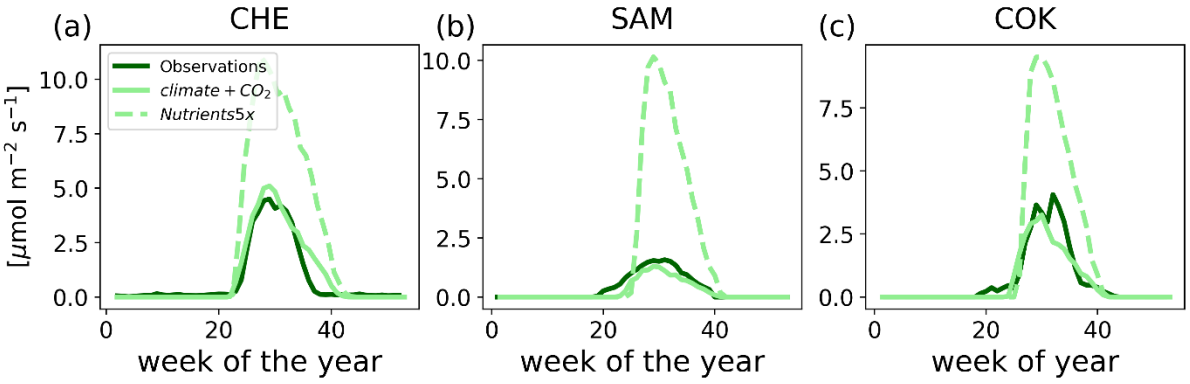

Figure S7. Weekly means from the *climate+CO₂* simulation plotted against the simulation Nutrients5x, where soil N and P were initialized at 5-fold the values from *climate+CO2,* simulated at the sites Cherskiy (CHE), Samoylov (SAM) and Chokurdakh (COK).

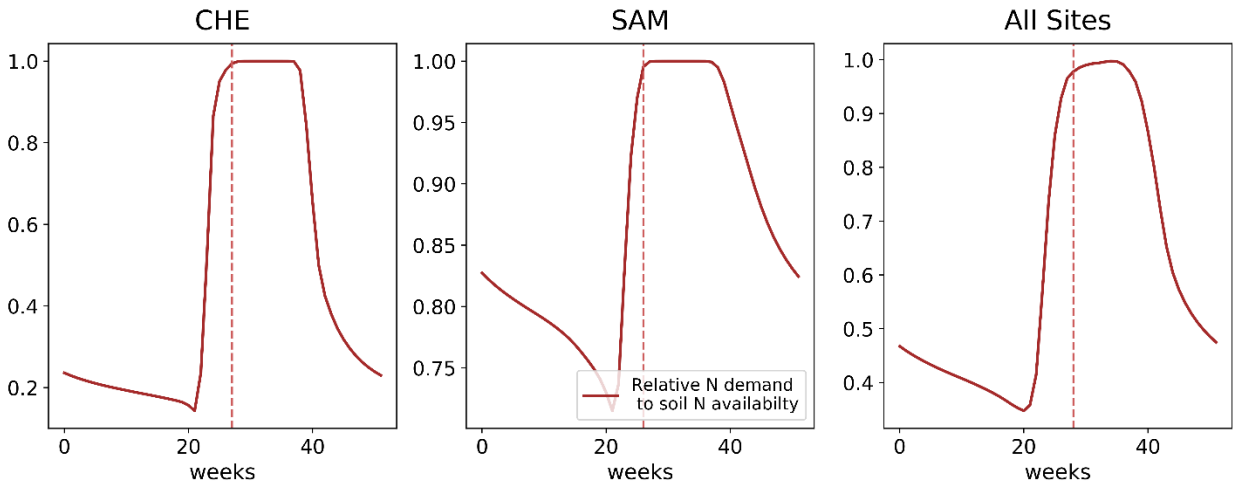

Figure S8. Relative plant N demand to soil N availability at Cherskiy (CHE), Samoylov (SAM) and over all high-Arctic sites, respectively.

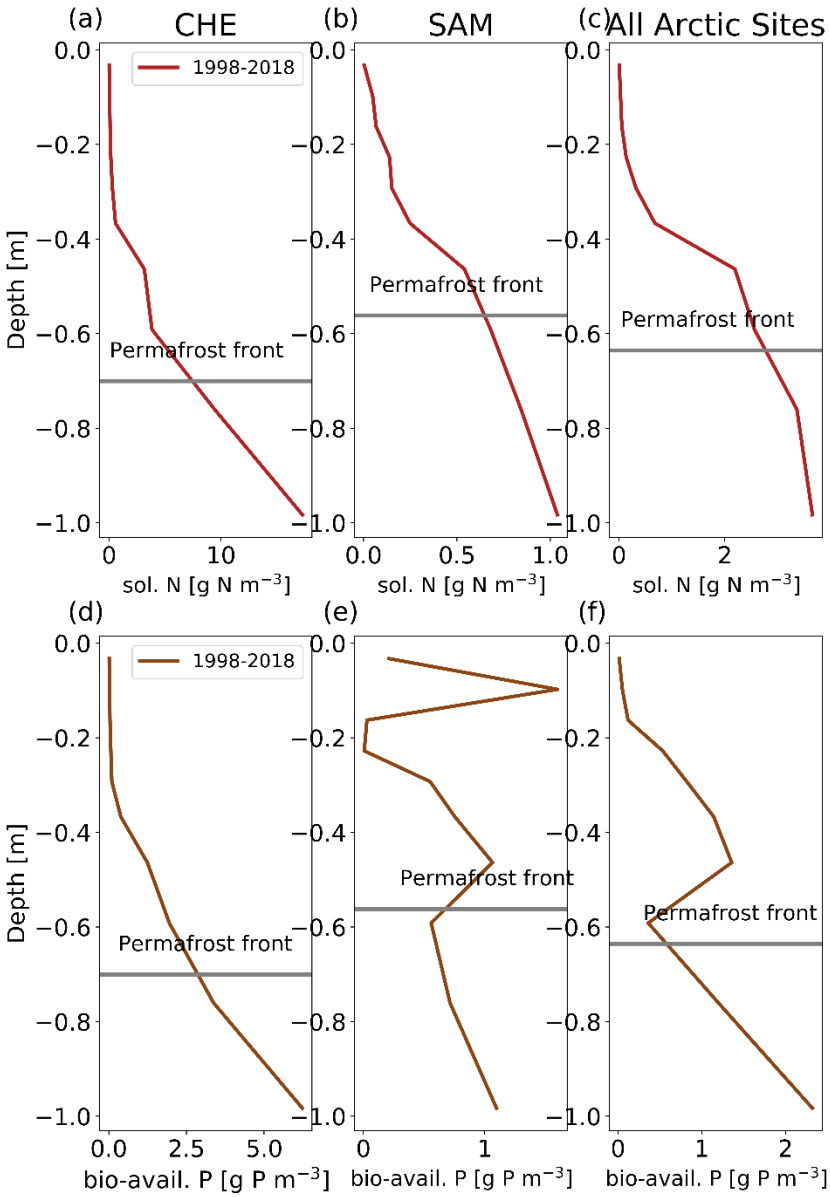

Supplement S9. Annual mean vertical profiles of (panels a,b,c) inorganic nitrogen (sol. N), meaning solute NH_4^+ + NO_3^-, and biologically available (solute and weakly bound to mineral) phosphorus (panels d,e,f) at Cherskiy (CHE), Samoylov (SAM) and Chokurdakh (COK) sites averaged over 1998-2018 in simulation *climate+CO_2*.

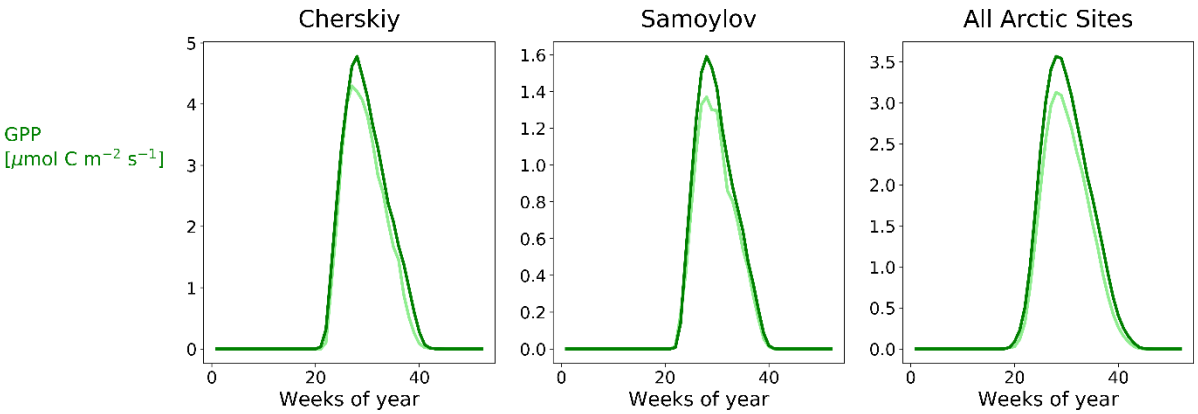

Figure S10. Weekly mean simulated GPP (*climate+CO_2* simulation) averaged for 1950-1970 (light green) and for 1998-2018 (dark green) at Cherskiy, Samoylov and averaged over all Arctic sites.

Supplement Tables

Supplement Table S1. QUINCY parameters that were introduced or change for a better representation of high latitude processes, with process equations available in Supplementary Information of Thum et al., 2019.

Biogeochemical parameters	**Value and unit**
Soil Organic Matter Turnover Times	
Polymeric Litter	0.033 yr^{-1}
Structural Litter	0.124 yr^{-1}
Fast Soil Organic Matter	2 yr^{-1}
Slow Organic Matter	100 yr^{-1}
Temperature of peak decomposition rate	315.15 K
Activation Energy for decomposition	53000 $Jmol^{-1}$
De-activation Energy for decomposition	100000 $Jmol^{-1}$
Minimum water potential for decomposition	-2.0 MPa
Plant Uptake	
Temperature of peak uptake	313.15
Activation Energy for uptake	53000 $Jmol^{-1}$
De-activation Energy for uptake	100000 $Jmol^{-1}$
Low-affinity uptake parameter NH4	0.0416 m^3 mol^{-1}
Low-affinity uptake parameter NO3	0.0416 m^3 mol^{-1}
High-affinity uptake parameter NH4	1.0
High-affinity uptake parameter NO3	1.0
Activation energy of half saturation point	30000 J mol
Scaling factor for the sensitivity of half-saturation constant to moisture limitation	0.001
Fraction of target labile N at which uptake is reduced to 50 %	0.75
Nutrient uptake response function to labile nutrient concentration	2.0
Maximum sum of NH4 and NO3 at which biological nitrogen fixation occurs	0.05 mol N m^{-2}
Maximum rate of biological nitrogen fixation	0.005 mol N m^{-2} s^{-1}
Nitrification and Denitrification	
Λ of Weibull function to relate anaerobic volume fraction to soil moisture	1.3
K of Weibull function to relate anaerobic volume fraction to soil moisture	3.0
Maximum nitrification rate	0.4 day^{-1}
Activation energy of nitrification	80000 J mol^{-1}
De-activation energy of nitrification	200000 J mol^{-1}
Optimum temperature for nitrification	311.15 K
Fraction of nitrification lost to NO_y	0.02
Fraction of nitrification lost to N_2O	0.002
Activation energy of denitrification	47000 J mol^{-1}
Maximum denitrification rate	0.1 day^{-1}
Half-saturation constant C of denitrification	20.0 mol m^{-3}
Half-saturation constant NO_3 of denitrification	1162.6 mol m^{-3}
Fraction of denitrification lost to NO_y	0.002
Fraction of denitrification lost to N_2O	0.02
Activation energy of gas diffusion	47000 K mol^{-1}

Supplement Table S2. QUINCY parameters that were introduced or change for a better representation of high latitude processes.

Soil physics parameters	**Original setting**	**Updated setting**
heat conductivity unfrozen organic [W m^{-1} K^{-1}]	-	1.4
heat conductivity unfrozen mineral [W m^{-1} K^{-1}]	2.0	2.0
heat conductivity frozen organic [W m^{-1} K^{-1}]	-	0.8
heat conductivity frozen mineral [W m^{-1} K^{-1}]	-	1.4
heat capacity unfrozen organic [J Kg^{-1} K^{-1}]	-	2300
heat capacity unfrozen mineral [J Kg^{-1} K^{-1}]	2000	2000
heat capacity frozen organic [J Kg^{-1} K^{-1}]	-	2300
heat capacity frozen mineral [J Kg^{-1} K^{-1}]	-	2000
Supercooled water to field capacity ratio [-]	-	0.2
Water density [kg m^{-3}]	998	998
Ice density [kg m^{-3}]	-	916.7
Snow parameters		
Albedo VIS & NIR[-]	-	0.6
Snow density [kg m^{-3}]	-	100
Snow heat capacity [J Kg^{-1} K^{-1}]	-	2200
Snow heat conductivity [W m^{-1} K^{-1}]	-	0.14
Snow albedo [-]	-	0.8
Minimum threshold for snow to impact soil surface heat budget [m]	-	0.02
Maximum thickness of individual snow layers [m]	-	0.05
Vegetation parameters		
Growth degree day (GDD) threshold [° days]	20	30
Senescence temperature [°C]	0	4.0
Minimum growing days before which senescence can take place [d]	10	30

Supplement Table S3: Soil bulk weight, N and C ratios of soil samples collected at Cherskiy.

Depths	Bulk weight [mg]	N [%]	C [%]
01, 3 - 5 cm	21,24	1,33	37,89
02, 18 cm	22,38	1,84	31,00
03, 30 cm	20,51	1,68	25,35
04, 33 cm	33,17	0,14	2,09
05, 45 cm	33,53	0,17	2,51
06, 60 cm	35,53	0,14	2,12
07, 68 cm	74,11	0,17	2,41
08, 88 cm	74,73	0,28	4,05
09, 100 cm	80,27	0,26	3,61
10, 113 cm	80,64	0,27	3,49
11, 120cm	79,99	0,16	1,79
12, 138cm	81,81	0,15	1,74
13, 165cm	83,01	0,16	1,87
14, 180cm	80,71	0,14	1,58
15, 200cm	80,92	0,17	2,13
16, 227cm	81,98	0,11	1,20
17, 255cm	81,33	0,15	1,69
18, 287cm	82,49	0,17	2,07
19, 295cm	82,17	0,11	1,28
20, 318cm	81,68	0,19	2,16
21, 338cm	81,22	0,15	1,58
22, 360cm	82,21	0,07	0,60
23, 380cm	83,07	0,15	1,65
24, 395cm	105,42	0,18	2,09
25, 405cm	104,63	0,07	0,65
26, 418cm	109,02	0,11	1,37
27, 465cm	107,32	0,06	0,72
28, 475cm	99,65	0,15	1,72
29, 495cm	111,83	0,07	0,63
30, 505cm	111,80	0,08	0,75

Supplementary Information: References

Holl, D., Pancotto, V., Heger, A., Camargo, S. J., and Kutzbach, L.: Cushion bogs are stronger carbon dioxide net sinks than moss-dominated bogs as revealed by eddy covariance measurements on Tierra del Fuego, Argentina, Biogeosciences, 16, 3397–3423, https://doi.org/10.5194/bg-16-3397-2019, 2019a.

Holl, D., Wille, C., Sachs, T., Schreiber, P., Runkle, B. R. K., Beckebanze, L., Langer, M., Boike, J., Pfeiffer, E.-M., Fedorova, I., Bolshianov, D. Y., Grigoriev, M. N., and Kutzbach, L.: A long-term (2002 to 2017) record of closed-path and open-path eddy covariance CO2 net ecosystem exchange fluxes from the Siberian Arctic, Earth Syst. Sci. Data, 11, 221–240, https://doi.org/10.5194/essd-11-221-2019, 2019b.

Holl, D., Pfeiffer, E.-M., and Kutzbach, L.: Comparison of eddy covariance CO_2 and CH_4 fluxes from mined and recently rewetted sections in a northwestern German cutover bog, Biogeosciences, 17, 2853–2874, https://doi.org/10.5194/bg-17-2853-2020, 2020.

Pallandt, M. M. T. A., Kumar, J., Mauritz, M., Schuur, E. A. G., Virkkala, A.-M., Celis, G., Hoffman, F. M., and Göckede, M.: Representativeness assessment of the pan-Arctic eddy covariance site network and optimized future enhancements, Biogeosciences, 19, 559–583, https://doi.org/10.5194/bg-19-559-2022, 2022.

Runkle, B. R. K., Sachs, T., Wille, C., Pfeiffer, E.-M., and Kutzbach, L.: Bulk partitioning the growing season net ecosystem exchange of CO2 in Siberian tundra reveals the seasonality of ist carbon sequestration strength, Biogeosciences, 10, 1337–1349, https://doi.org/10.5194/bg-10-1337-2013, 2013.

Walvoord, M.A. and Kurylyk, B.L.: Hydrologic impacts of thawing permafrost: a review. *Vadose Zone J.,* 15 (2016), pp. 1-20.